Elastic Full Waveform Inversion of Vertical Seismic Profile data acquired with Distributed Acoustic Sensors

Running Head: FWI of DAS VSP data

Anton Egorov[1,2,4], Julia Correa[1,2], Andrej Bóna[1,2], Roman Pevzner[1,2], Konstantin Tertyshnikov[1,2], Stanislav Glubokovskikh[1,2], Vladimir Puzyrev[1], Boris Gurevich[1,2,3]

[1]*Curtin University, GPO Box U1987*

Perth, WA 6845, Australia

[2]*CO2CRC*

PO Box 1182, Carlton, VIC 3053, Australia

[3]*CSIRO*

Australian Resources Research Centre, 26 Dick Perry Avenue, Kensington, WA 6151, Australia

[4]*Lomonosov Moscow State University*

ul. Leninskiye Gory, 1, Moscow, 119991, Russia

Contacts: Anton Egorov, anton.egorov@postgrad.curtin.edu.au

KEYWORDS

Vertical seismic profile (VSP), full-waveform inversion, borehole geophysics, fiber-optic sensors

ABSTRACT

Distributed acoustic sensing (DAS) is a rapidly developing technology particularly useful for the acquisition of vertical seismic profile (VSP) surveys. DAS data are increasingly used for seismic imaging, but not for estimating rock properties. We propose a workflow for estimating elastic properties of the subsurface using full waveform inversion (FWI) of DAS VSP data. Whereas conventional borehole geophones usually measure three components of particle velocity, DAS measures a single quantity, which is an approximation of the strain or strain rate along the fiber. Standard FWI algorithms are developed for particle velocity data, and hence their application to DAS data requires conversion of these data to particle velocity along the fiber. This conversion can be accomplished by a specially designed filter. Field measurements show that the conversion result is close to vertical particle velocity as measured by geophones. Elastic time-domain FWI of a synthetic multi-offset VSP dataset for a vertical well shows that the inversion of the vertical component alone is sufficient to recover elastic properties of the subsurface. Application of the proposed workflow to a multi-offset DAS dataset acquired at the CO2CRC Otway Project site in Victoria, Australia reveals salient subhorizontal layering consistent with known geology of the site. The inverted V_P model at the well location matches the upscaled V_P log with a correlation coefficient of 0.85.

INTRODUCTION

Distributed acoustic sensing (DAS) is a novel data acquisition solution; a technology that enables the recording of seismic data using fiber-optic cables instead of traditional sensors such as geophones and hydrophones. Seismic waves propagating through the subsurface deform the fiber-optic cable, causing strain, and that strain is recorded using the backscattering of laser pulses (Posey et al., 2000). DAS systems are insensitive to the compressional waves whose displacement is normal to the fiber (Kuvshinov, 2016). The seismic reflection method is most commonly used to image subhorizontal interfaces, and hence relies on compressional waves propagating in the direction close to the vertical. Thus, the directivity of DAS limits its potential application in surface seismic scenarios with horizontal cables and compressional waves. However this directivity issue is not a serious limitation for Vertical Seismic Profile (VSP) geometries, as in VSP most of these waves propagate along the well, where the DAS cable is deployed. Since permanent installation of DAS cable is possible, it can be conveniently used for time-lapse reservoir monitoring. Several successful applications of DAS VSP as a tool for subsurface imaging have been reported, particularly for reservoir monitoring (Mateeva et al., 2014; Daley et al., 2016).

In most published studies, DAS VSP data are analysed using conventional VSP imaging techniques. While these methods provide information on the structure of the subsurface, they do not supply any quantitative estimates of the physical properties. Full Waveform Inversion (FWI) is a powerful alternative to these imaging methods. FWI aims to estimate spatial distribution of physical properties using the seismic data (Virieux and Operto, 2009). FWI has been successfully applied to field VSP datasets acquired with geophones (Owusu et al., 2016; Charara et al., 1996), and has demonstrated its potential for estimating the time-lapse changes in the elastic properties from VSP data (Egorov et al., 2017; Liang et al., 2013).

Our objective is to apply elastic 2D FWI to an onshore VSP dataset acquired with a DAS recording system and a Vibroseis source. Existing FWI methodologies use input pressure or particle velocity recordings, and hence cannot be directly applied to DAS measurements. While a new inversion technology may be developed that will directly use the strain measurements supplied by DAS (e.g., Podgornova et al., 2017), we opt for converting DAS recordings to the particle velocity along the fiber instead (Bóna et al., 2017). This allows us to employ existing FWI algorithms and workflows designed for conventional geophone data. We conduct a detailed comparison of the converted DAS data and vertical component geophone data acquired in the same well to outline the limitations of the conversion technique. After that, we discuss the FWI workflow and demonstrate its capabilities on a synthetic dataset designed to replicate the field example. We then apply the same workflow to a DAS field dataset acquired at the CO2CRC Otway site, Victoria, Australia during May, 2017.

DATA

We illustrate our workflow with the field data acquired in CO2CRC Otway site, located 240 km South-West of Melbourne, Victoria, Australia. The dataset was acquired for the characterization of the subsurface around the recently drilled CRC-3 well. CRC-3 is a planned injector well for Stage 3 of the CO2CRC Otway Project, a pilot CO_2 sequestration project partly aimed at testing and validating a number of sequestration monitoring techniques, including VSP acquired with DAS. The detailed acquisition configuration and signal-to-noise characteristics of the data are described by Correa et al. (2017). The well is instrumented with a number of different types of fiber optic cables. We use the VSP gathers acquired with a fiber cable that was cemented behind the steel well casing. We employ an interrogator with optimized architecture and a fiber optic cable specifically engineered to provide stronger backscattered signal. The gauge length is 10 m, the depth sampling in raw

DAS data is 1 m. These features of the acquisition provide sufficient signal-to-noise ratio (approximately 35 dB), which allows inversion of single-sweep shot records acquired with no repeats. A 26,000 lb seismic vibrator truck was used as a source. Shots used in the inversion were extracted from a walkaway survey conducted on site; their locations are displayed in red in Figure 1. Raw single-sweep DAS gathers used in the inversion are shown in Figure 2.

To apply the FWI to DAS data, we first convert these data to particle velocity, and compare the result with a conventional clamped geophone seismic gather acquired in the same steel-cased well. The shot point used for the demonstration of DAS conversion is displayed in purple in Figure 1.

APPROACH

Conversion of DAS data to particle velocity

DAS systems measure strain or strain rate, a temporal derivative of strain (Parker et al., 2014). Figure 3 shows a schematic diagram of a DAS measurement. The result of DAS measurement at $z = 0$ is the difference between the cable displacements integrated over two laser pulses (which are displayed as Gaussian windows). Here, we assume perfect coupling between the fiber and the well. The DAS response can be written as (Bóna et al., 2017):

$$D(z,t) = \frac{d}{dt} \int_{-\infty}^{+\infty} (u(z - G/2 + l,t) - u(z + G/2 + l,t)) w(l) dl \,, \tag{1}$$

where u is the displacement along the direction of the fiber, Z axis follows the fiber, t is time, G is the gauge length, $w(l)$ is shape of the laser pulse. As in our case the well is vertical, Z in the equations below corresponds to depth.

From equation (1), the DAS response to the monochromatic plane wave $Ae^{-i(\omega t - \mathbf{kx})}$ is:

$$D(z,t) = \frac{d}{dt} \int_{-\infty}^{+\infty} (A_z e^{-i(\omega t - k_z (z+l-G/2))} - A_z e^{-i(\omega t - k_z (z+l+G/2))}) w(l) dl \,, \tag{2}$$

where **k** is the wavenumber, ω is the angular frequency.

We assume that the light pulse is a box with the pulse width *L* (orange line in Figure 3 shows box approximations for each of the displayed pulses). For this approximation, the shape function $w(l)$ is equal to 1 on the segment [*-L/2 L/2*] and equal to 0 everywhere else. In this case, equation (2) gives:

$$D(z,t) = A_z e^{-i(\omega t - k_z z)} \frac{\omega}{k_z} (e^{ik_z L/2} - e^{-ik_z L/2})(e^{ik_z G/2} - e^{-ik_z G/2}) \cdot \quad (3)$$

The vertical component of the particle velocity of the same plane wave is:

$$G(z,t) = -i\omega A_z e^{-i(\omega t - k_z z)} \cdot \quad (4)$$

The ratio of equations (4) to (3) provides a filter that converts DAS response to the particle velocity along the path of the fiber:

$$F(k_z) = \frac{-ik_z}{(e^{ik_z L/2} - e^{-ik_z L/2})(e^{ik_z G/2} - e^{-ik_z G/2})} = \frac{ik_z}{4\sin(k_z L/2)\sin(k_z G/2)} \cdot \quad (5)$$

As the filter (5) might have zero values in the denominator, it is convenient to regularize it as follows (Hatton et al., 1986):

$$F_{REG}(k_z) = \frac{ik_z}{4\sin(k_z L/2)\sin(k_z G/2) + \gamma}, \quad (6)$$

where γ is the regularization coefficient, which is chosen as a small positive number. The filter $F_{REG}(k_z)$ should be applied to the data in the vertical wavenumber domain, i.e., after Fourier transformation along the Z axis. We used an arbitrary plane wave in the derivation, so any event, that can be decomposed using the plane-wave basis, will be processed correctly due to superposition principle. The conversion approach described above is similar to a number of other methods (e.g., Bakku, 2015; Dean et al., 2017). Regularization and

capability of taking into account the pulse width are the distinguishing features of our technique.

In Figure 4, we compare DAS gathers with the reference geophone data acquired in the same well during the same survey. It can be seen that the raw DAS gather (Figure 4a) and the geophone gather (Figure 4b) have different wavelet shapes. Note that the DAS gather has a defect in the fiber at approximately 1400 m depth, which occurred during the production process; the traces in the damaged part are zeroed. Furthermore, it is known that the upgoing wavefields in DAS and geophone data have opposite polarities (Daley et al., 2016). Conversion of DAS to the particle velocity without regularization (Figure 4c) corrects for the wavelet shape and the polarity of the upgoing events. In a noise-free case, the operator expressed by equation (5) would not require any regularization. However, on this noisy field dataset, unregularized conversion strongly amplifies the noise components with low k_z values, as the correction filter has a singularity at $k_z = 0$. On the gather, this noise shows as spurious events with near-infinite apparent velocity. Filtering with a regularization coefficient $\gamma = 0.0005$ attenuates those events (Figure 4d); however the filter fails to reconstruct the arrival of the source-generated S-wave with near-infinite apparent velocity (the event highlighted with a green rectangle). The traces of the corrected DAS gather with $\gamma = 0.0005$ match the geophone traces (Figure 5). Increasing the regularization coefficient to $\gamma = 0.05$ leads to the attenuation of low wavenumbers in the filtering result, and hence the converted gather (Figure 4e) resembles the raw DAS data more than the geophone data. More generally, our filter takes into account the directivity of the DAS signal but in the obtained particle velocity this directivity still manifests itself as the dependence of the signal-to-noise ratio on the arrival angle.

Still, the converted DAS gather in Figure 4d does not exactly match the geophone gather, which can be observed in Figure 5. We were able to construct a shaping filter using Wiener filtering theory (Claerbout, 1985) to match the converted gather in Figure 4d to the geophone gather. The white noise regularization parameter in the matching filter was set to 10^{-6}. The matched gather is shown in Figure 4f. The average correlation coefficient between the traces in the geophone gather and respective traces in the matched gather is 0.9. The match between traces can be observed in Figure 5, a match between the amplitude spectra can be seen in Figure 4h.

A single matching filter with 100 ms length was used for all the traces in the gather. Thus, the difference between the original unmatched converted gather and the geophone gather is mostly in the wavelet shape, additional to the unsatisfactory conversion of the events with near-infinite apparent velocity.

In order to explain the differences in the wavelet shape, we compare the amplitude and phase characteristics of such shaping filters for several shots in the survey to the amplitude and phase characteristics of the geophones similar to the geophones used during the survey (Figure 6). Above the expected minimum frequency of the signal (8 Hz, which is marked with the dashed red line) the shaping filters replicate the shape of the geophone characteristics. For far offsets (1025 and 2000 m), the amplitude characteristics of the filters are different from the geophone amplitude response at high frequencies, which we attribute to low signal-to-noise ratio at those frequencies due to anelastic attenuation.

This suggests that the converted DAS gathers represent a measurement of particle velocity that is, in a certain sense, more accurate than standard geophones. This is confirmed by the fact that the wavelet in the first arrivals of the converted DAS gather (red line in Figure 5) is more symmetric and closer to the zero-phase sweep autocorrelation than the wavelet in the

first arrivals of the geophone gather (blue curve in Figure 5). Thus, the difference in wavelet between the converted DAS gather and the geophone gather is not due to the inaccuracy of the conversion, but due to specific characteristics of the amplitude and phase response of the geophones. Thus, the failure of the conversion to reconstruct the events with near-infinite apparent velocity remains its only limitation, which can be observed on the difference between the geophone and corrected matched DAS gathers (Figure 4g). This limitation is related to the fundamental physical constraints of DAS systems.

Choosing the regularization coefficient is subjective. The process of choosing this parameter is outlined by Correa et al. (2017). It involves starting with a very small γ (almost unregularized) and increasing it gradually. Each conversion result is compared to the unregularized conversion result. The 'optimal' coefficient provides the attenuation of the conversion noise, while preserving the seismic events and waveforms of the unregularized result. For the inversion, we use the converted gather with a regularization coefficient $\gamma = 0.0005$. As a part of the source-generated S-wave arrivals was not reconstructed, we remove the source-generated S-wave from the inversion by time windowing (muting). Furthermore, the frequency content of the source-generated S-waves and the P-waves is different, that is, S-waves lack the high frequencies that P-waves have. This may be related to complex effects in the near-field of the source or the finite-source effect. Both of these phenomena cannot be explained by elastic modeling with a vertical force source that we use for FWI, which is another reason to remove these events from the inversion.

Inversion workflow

After the DAS gather is converted to the vertical component of particle velocity, it can be inverted with the traditional least-squares FWI (Tarantola, 1984). In this section, we

summarize our FWI workflow and demonstrate its application on synthetic and field data examples.

Our FWI workflow is similar to the workflow for the inversion of geophone VSP data (Egorov et al., 2017). We use a time-domain open-source software package IFOS2D (Köhn, 2011). The forward problem is solved using an elastic eight-order finite-difference staggered grid algorithm (Virieux, 1986; Bohlen and Saenger, 2006) with a cell size of 2.5 m. Limited-memory Broyden-Fletcher-Goldfarb-Shanno (L-BFGS) algorithm is used for optimization (Nocedal and Wright, 2006). L-BFGS is used instead of a more common conjugate gradient method due to its faster convergence and improved performance in case of multiparameter inversions (Brossier et al., 2009). We choose to parameterize the elastic inversion with V_P, V_S and density; though alternative parameterizations may be considered (e.g., Köhn et al., 2012). All three medium parameters are updated from the first iteration. Inversion for the wavelet shape is not carried out during the inversion, but the absolute amplitude of the wavelet is estimated at each iteration. We estimate the source wavelet from the recorded direct arrivals. For the inversion, we did not apply any wavelet estimation techniques or data processing procedures, such as deconvolution (Pratt, 1999). The starting model is 1D and is obtained by smoothing and extrapolating the available log data and the velocities from first breaks on the checkshot.

To reduce the nonlinearity of the inverse problem, we employ the multiscale approach (Bunks et al., 1995) using high-cut Butterworth filters. At the first iteration, the filter slope is placed at 14 Hz. This slope is then shifted to 80 Hz in 1 Hz steps. A step is made each time the misfit change between two consequent iterations is small enough (10% in our case). On the average, each frequency step takes about 10-15 iterations to finish. No regularization is used during the inversion, only the L2 misfit functional is being optimized. The smoothness of the output model is not constrained, however the inverted model is smoothed using a 2D

Gaussian spatial filter once every 20 Hz, which helps to weaken the receiver-side artefacts. The standard deviation of the smoothing kernel is 2.5 m in the vertical direction and 10 m in the horizontal direction. Gradient preconditioning is performed by the approximation of the inverse Hessian matrix provided by the L-BFGS optimization method (Nocedal and Wright, 2006). Furthermore, we apply semi-circular tapers to the gradients around the source locations (the radius of each taper is 80 m), which allows us to suppress the inversion artefacts in the near field of the source. According to our experiments, these tapers do not significantly influence the inverted models away from the sources.

To demonstrate applicability of elastic FWI to DAS data, we tested several variants of the inversion workflow, and chose the one that produced the subjectively 'clearest' result. This result can probably be improved. Our workflow can be applied to other similar VSP datasets.

SYNTHETIC DATA EXAMPLE

To test our workflow, we compute the vertical component of particle velocity for corresponding offset VSP gathers using 2D finite-difference time-domain approach and invert them. The model we use was designed to replicate the geological conditions of the Otway site (Glubokovskikh et al., 2016), where the field dataset was acquired. The acquisition geometry is similar to the actual field geometry. The receivers are located at depths from 270 to 1750 m with 5 m spacing. Seven shot points with offsets from 450 to 900 m are used for the inversion.

Inversion results are compared to the true and initial models in Figure 7. Here, we present the inversion results both with and without the source-generated S-wave. It can be seen that the inversion updates are roughly limited to the region bounded by the well, the free surface and the straight line between the deepest receiver and the farthest source. The main changes occur close to the well, in the displayed window, where inversion identified several thin layers.

Slight lateral variations of the subsurface structure are also captured in this part of the model. Overall, the inverted models in the updated region are consistent with the true structure of the medium.

Qualitatively, the V_P inversion results are similar for inversions with and without the source-generated S-wave. Their root-mean-square deviation (RMSD) from the true V_P model is 111 and 118 m/s respectively. The density and V_S results for these two inversions differ mainly further away from the well and at small depths. RMSD values show that the inversion result with source S-waves is closer to the true model (Figure 7). Unfortunately, as discussed in previous sections, in our field data example we have to exclude source-generated S-waves from the inversion due to the limitations of our conversion technique and significant difference in frequency content between P and S-waves generated by the Vibroseis source in the field.

To examine the robustness of the workflow, we also conducted an inversion test with noisy synthetic. To simulate DAS acquisition, the modeled gathers were converted to DAS response using the inverse of filter (5), without regularization. After conversion, we added white noise with signal-to-noise ratio of 30 dB (which is lower than in our field dataset), and then converted back to particle velocity using the regularized filter (6). The inversion result for this dataset (not shown) looks exactly the same as the one displayed in Figure 7(d, h, l).

FIELD DATA EXAMPLE

The same FWI workflow is applied to the Otway field DAS multi-offset Vibroseis VSP dataset. Input into the inversion comprises traces acquired at depths from 310 to 1640 m with 5 m spacing from six shot points with offsets from 500 to 870 m. Before the inversion, these data are subjected to a number of pre-processing steps. First, we correlate the raw gathers with the sweep signal. Second, we convert the gathers to particle velocity along the path of

the fiber, as described above. Third, we apply a deterministic phase-shifting filter to convert the zero-phase correlated wavelet in the data to a minimum-phase wavelet for convenience (Gibson and Larner, 1984). As all the shots involved in the inversion were acquired on a solid ground (a road surface), the wavelet in the data is very stable. This allows us to estimate a single wavelet using the downgoing wavefield from all shots, and use this wavelet in the inversion. Finally, we convert the gathers in the dataset to approximate 2D amplitudes (Pica et al., 1990).

The field data inversion results are shown in Figure 8. It can be seen that the V_P inverted model contains subhorizontal layers that resemble sedimentary geological structure of the survey site. It appears that these layers are true features of the subsurface. In the V_S and density models, such layers can be seen only in the upper part of the medium. Some lateral variations of model properties were also identified by the inversion. It is unclear whether these variations are the true features of the site. More definitive information about lateral variations of rock properties requires broader source coverage.

Comparison of the inverted V_P model with the available log data (Figure 8g) shows that the inversion is generally able to reconstruct the velocity structure of the medium. The mismatch at approximately 1350 to 1400 m is caused by a defect in the fiber which forced us to remove a number of traces from the inversion at this depth. The correlation coefficient between the displayed smoothed V_P log and the inverted V_P near the well is equal to 0.85. We believe that using a more comprehensive survey geometry (for example, source offsets smaller than 420 m and sources on the other side of the well) could improve the match between the log and the model (for example, in the interval between 950 and 1050 m). At the current stage of our research, we do not analyse the S-wave velocity and density inversion results apart from performing visual analysis. The study of these properties and improvement of these models is the subject of future research.

Figure 9 shows a comparison of a converted field DAS gather, a synthetic gather calculated in the final inverted model and their misfit at the maximum inversion frequency. A number of traces at the top and bottom of the gather and around the defect in the fiber had to be removed from the inversion due to the edge effects of the filter $F_{REG}(k_z)$. Overall, a good match can be observed within the displayed inversion window, the energy of the misfit is 8% of the field gather's energy. On the misfit plot (Figure 9c), the converted S-waves (black arrow) and the upgoing waves from below the well bottom (white arrow) have highest values, which means that they are not well explained by the inverted models. The quality of the output S-wave velocity model remains in question due to the fact that the source S-waves were not used in the inversion, and their role is yet to be clarified.

The models of subsurface properties obtained using the presented FWI workflow can be used for reservoir characterization. The results obtained with this workflow will also be used, in conjunction with the log data (available in the depth interval from 920 to 1650 m), to construct baseline models for the monitoring of CO_2 injection in the Stage 3 of the Otway Project. The workflow for application of FWI to time-lapse borehole seismic data for monitoring CO_2 sequestration is outlined by Egorov et al. (2017).

CONCLUSIONS

Our results show that VSP data acquired with DAS recording systems may be converted to the particle velocity along the fiber. We present a regularized conversion algorithm that corrects for the pulse width and gauge length and study its properties. We compare the converted DAS gather to the geophone gather and show that the remaining differences between the waveforms occur either due to physical limitations of DAS (low sensitivity of DAS to the events that arrive normal to the fiber) or due to the complexity of the geophone

response relative to the particle velocity. The quality of the conversion allows us to conduct FWI on converted data in order to obtain quantitative estimates of the medium properties.

We apply conventional elastic FWI to the converted data excluding the source-generated S-wave from the field data inversion. In the field data, these waves lack high frequencies, possibly due to complex wave propagation in the near-field of the source. Not including this wave into the inversion leads to poor quality of recovered S-wave velocity and density models. However, the workflow still provides a realistic estimate of P-wave velocity, which we corroborate on synthetic data. The P-wave velocity model estimated by FWI of field VSP dataset acquired with DAS recording system contains salient subhorizontal layering, which matches with other data available for the site. The match between the recovered P-wave velocity model and the P-wave velocity log is affected by the fact that this FWI workflow is not constrained by the log data, but it is still reasonable in most parts of the available log. Here, we are only interpreting the P-wave velocity model obtained from our measurements. The improvement of S-wave velocity and density models will be the subject of our future work. Reliable estimation of S-velocity is essential for making quantitative interpretation of VSP data. Our synthetic test shows that for this purpose, it would be very useful to use not only converted S-waves, but also the source-generated S-wave.

Our study shows that FWI of DAS VSP data is feasible. As DAS is often used for reservoir monitoring, the presented workflow can be applied to build the baseline model of the subsurface. As a CO_2 injection is planned in Otway during Stage 3 of the Otway Project, time-lapse FWI of DAS VSP data is one of the intended next steps of our research.

ACKNOWLEDGEMENTS

The Otway Project received CO2CRC funding through its industry members and research partners, the Australian Government under the CCS Flagships Programme, the Victorian

State Government and the Global CCS Institute. The authors wish to acknowledge financial assistance provided through Australian National Low Emissions Coal Research and Development (ANLEC R&D) supported by the Australian Coal Association Low Emissions Technology Limited and the Australian Government through the Clean Energy Initiative. We would also like to thank the Pawsey Supercomputing Centre for providing the computational resources and the authors of the IFOS FWI package for the codes that allow elastic FWI of VSP data. We want to thank Paul Wellington for useful discussions concerning our FWI workflow. We are grateful to Andy Clarke and Tom Parker (Silixa), for the advice on well instrumentation and DAS data acquisition.

REFERENCES

Bakku, S. K., 2015, Fracture characterization from seismic measurements in a borehole: Ph. D. thesis, Massachusetts Institute of Technology.

Bohlen, T., and E. H. Saenger, 2006, Accuracy of heterogeneous staggered-grid finite-difference modeling of Rayleigh waves: Geophysics, **71**, no. 4, T109-T115. doi: 10.1190/1.2213051.

Brossier, R., S. Operto, and J. Virieux, 2009, Seismic imaging of complex onshore structures by 2D elastic frequency-domain full-waveform inversion: Geophysics, **74**, no. 6, WCC105-WCC118. doi: 10.1190/1.3215771.

Bunks, C., F. M. Saleck, S. Zaleski, and G. Chavent, 1995, Multiscale seismic waveform inversion: Geophysics, **60**, no. 5, 1457-1473. doi: 10.1190/1.1443880.

Bóna, A., T. Dean, J. Correa, R. Pevzner, K. Tertyshnikov, and L. Van Zaanen, 2017, Amplitude and Phase Response of DAS Receivers: 79th Conference and Exhibition, EAGE, Extended Abstacts, We A5 13. doi: 10.3997/2214-4609.201701200.

Charara, M., C. Barnes, and A. Tarantola, 1996, The state of affairs in inversion of seismic data: An OVSP example: 66th Annual International Meeting, SEG, Expanded Abstracts, 1999-2002. doi: 10.1190/1.1826558.

Claerbout, J. F., 1985, Fundamentals of Geophysical Data Processing: With Applications to Petroleum Prospecting: Blackwell Scientific Publications.

Correa, J., A. Egorov, K. Tertyshnikov, A. Bona, R. Pevzner, T. Dean, B. Freifeld, and S. Marshall, 2017, Analysis of signal to noise and directivity characteristics of DAS VSP at near and far offsets — A CO2CRC Otway Project data example: The Leading Edge, **36**, no. 12, 994a991-994a997. doi: 10.1190/tle36120994a1.1.

Daley, T. M., D. E. Miller, K. Dodds, P. Cook, and B. M. Freifeld, 2016, Field testing of modular borehole monitoring with simultaneous distributed acoustic sensing and geophone vertical seismic profiles at Citronelle, Alabama: Geophysical Prospecting, **64**, no. 5, 1318-1334. doi: 10.1111/1365-2478.12324.

Dean, T., T. Cuny, and A. H. Hartog, 2017, The effect of gauge length on axially incident P-waves measured using fibre optic distributed vibration sensing: Geophysical Prospecting, **65**, no. 1, 184-193. doi: 10.1111/1365-2478.12419.

Egorov, A., R. Pevzner, A. Bóna, S. Glubokovskikh, V. Puzyrev, K. Tertyshnikov, and B. Gurevich, 2017, Time-lapse full waveform inversion of vertical seismic profile data: Workflow and application to the CO2CRC Otway project: Geophysical Research Letters, **44**, no. 14, 7211-7218. doi: 10.1002/2017GL074122.

Gibson, B., and K. Larner, 1984, Predictive deconvolution and the zero-phase source: Geophysics, **49**, no. 4, 379-397. doi: 10.1190/1.1441674.

Glubokovskikh, S., R. Pevzner, T. Dance, E. Caspari, D. Popik, V. Shulakova, and B. Gurevich, 2016, Seismic monitoring of CO_2 geosequestration: CO2CRC Otway case

study using full 4D FDTD approach: International Journal of Greenhouse Gas Control, **49**, 201-216. doi: 10.1016/j.ijggc.2016.02.022.

Hatton, L., J. Makin, and M. H. Worthington, 1986, Seismic data processing: theory and practice Blackwell Scientific.

Köhn, D., 2011, Time domain 2D elastic full waveform tomography: Ph. D. thesis, Christian-Albrechts-Universität zu Kiel.

Köhn, D., D. De Nil, A. Kurzmann, A. Przebindowska, and T. Bohlen, 2012, On the influence of model parametrization in elastic full waveform tomography: Geophysical Journal International, **191**, no. 1, 325-345. doi: 10.1111/j.1365-246X.2012.05633.x.

Kuvshinov, B. N., 2016, Interaction of helically wound fibre-optic cables with plane seismic waves: Geophysical Prospecting, **64**, no. 3, 671-688. doi: 10.1111/1365-2478.12303.

Liang, L., M. Li, R. Rufino, A. Abubakar, L. Nutt, H. Menkiti, S. Dummong, and R. Tøndel, 2013, Application of frequency-domain full-waveform inversion for time-lapse 3D VSP data interpretation: 83rd Annual International Meeting, SEG, Expanded Abstracts, 5107-5112. doi: 10.1190/segam2013-0989.1.

Mateeva, A., J. Lopez, H. Potters, J. Mestayer, B. Cox, D. Kiyashchenko, P. Wills, S. Grandi, K. Hornman, B. Kuvshinov, W. Berlang, Z. Yang, and R. Detomo, 2014, Distributed acoustic sensing for reservoir monitoring with vertical seismic profiling: Geophysical Prospecting, **62**, no. 4, 679-692. doi: 10.1111/1365-2478.12116.

Nocedal, J., and S. Wright, 2006, Numerical Optimization: Springer New York.

Owusu, J. C., O. Podgornova, M. Charara, S. Leaney, A. Campbell, S. Ali, I. Borodin, L. Nutt, and H. Menkiti, 2016, Anisotropic elastic full-waveform inversion of walkaway vertical seismic profiling data from the Arabian Gulf: Geophysical Prospecting, **64**, no. 1, 38-53. doi: 10.1111/1365-2478.12227.

Parker, T., S. Shatalin, and M. Farhadiroushan, 2014, Distributed Acoustic Sensing–a new tool for seismic applications: First Break, **32**, no. 2, 61-69. doi: 10.3997/1365-2397.2013034.

Pica, A., J. P. Diet, and A. Tarantola, 1990, Nonlinear inversion of seismic reflection data in a laterally invariant medium: Geophysics, **55**, no. 3, 284-292. doi: 10.1190/1.1442836.

Podgornova, O., S. Leaney, S. Zeroug, and L. Liang, 2017, On full-waveform modeling and inversion of fiber-optic VSP data: 87th Annual International Meeting, SEG, Expanded Abstracts, 6039-6043. doi: 10.1190/segam2017-17652912.1.

Posey, R., G. Johnson, and S. Vohra, 2000, Strain sensing based on coherent Rayleigh scattering in an optical fibre: Electronics Letters, **36**, no. 20, 1688-1689. doi: 10.1049/el:20001200.

Pratt, R. G., 1999, Seismic waveform inversion in the frequency domain, Part 1: Theory and verification in a physical scale model: Geophysics, **64**, no. 3, 888-901. doi: 10.1190/1.1444597.

Tarantola, A., 1984, Inversion of seismic reflection data in the acoustic approximation: Geophysics, **49**, no. 8, 1259-1266. doi: 10.1190/1.1441754.

Virieux, J., 1986, P-SV wave propagation in heterogeneous media: Velocity-stress finite-difference method: Geophysics, **51**, no. 4, 889-901. doi: 10.1190/1.1442147.

Virieux, J., and S. Operto, 2009, An overview of full-waveform inversion in exploration geophysics: Geophysics, **74**, no. 6, WCC1-WCC26. doi: 10.1190/1.3238367.

LIST OF CAPTIONS

Figure 1. Map of the survey site: shot points used for the inversion (red) and the shot point used to demonstrate DAS conversion (purple).

Figure 2. Raw DAS gathers used in the inversion.

Figure 3. Schematic of DAS measurement. G is the gauge length, L is the pulse width.

Figure 4. Comparison of DAS and vertical geophone gathers. Raw DAS gather (a); vertical geophone gather (b); DAS gather after conversion with $\gamma = 0$ (c), $\gamma = 0.0005$ (d), $\gamma = 0.05$ (e); DAS gather after conversion with $\gamma = 0.0005$ matched to geophone gather using a Wiener filter (f); difference between the geophone gather 4b and corrected matched DAS gather 4f decimated to geophone trace interval (g); and comparison of average amplitude spectra of gathers displayed in subplots 4b, 4d and 4f (h). The green box outlines an S-wave event which is not correctly recovered by the regularized conversion due to its low k_z value.

Figure 5. Comparison of geophone and DAS traces at the depth of 1500 m from Figure 4.

Figure 6. Comparison of amplitude (a) and phase (b) characteristics of the shaping filters for several shots of the survey (offsets of these shots are shown in the legend) and the amplitude and phase characteristics of the vertical geophones with 15 Hz natural frequency. For comparison, amplitude characteristics of the shaping filters were scaled with a constant scaling coefficient.

Figure 7. Inversion of synthetic data. V_P (a-d), V_S (e-h), and density (i-l) models of the subsurface: true (a, e and i), initial (b, f and j), inverted with source S-waves (c, g and k), and inverted without source S-waves (d, h and l). Source and receiver locations are overlayed on the models. RMSD values calculated in the displayed window are shown for each model.

Figure 8. Inversion of field data. Initial (a-c) and inverted (d-f) V_P (a, d), V_S (b,e), and density (c,f) models of the subsurface and a comparison of inverted V_P model 5 m away from the well with the available log data (g). In (g), V_P log is a dashed blue line, V_P log smoothed to approximate resolution of the inversion is a solid blue line, V_P starting model is shown in red and the V_P inverted model is shown in green. Receiver locations are overlayed on the models.

Figure 9. Converted DAS field gather at maximum inversion frequency (a), synthetic gather calculated in the final inverted model (b), and the misfit (c). On the misfit plot, the S-waves (black arrow) and the upgoing waves from below the wellbore (white arrow) have highest amplitudes.

Figure 1. Map of the survey site: shot points used for the inversion (red) and the shot point used to demonstrate DAS conversion (purple).

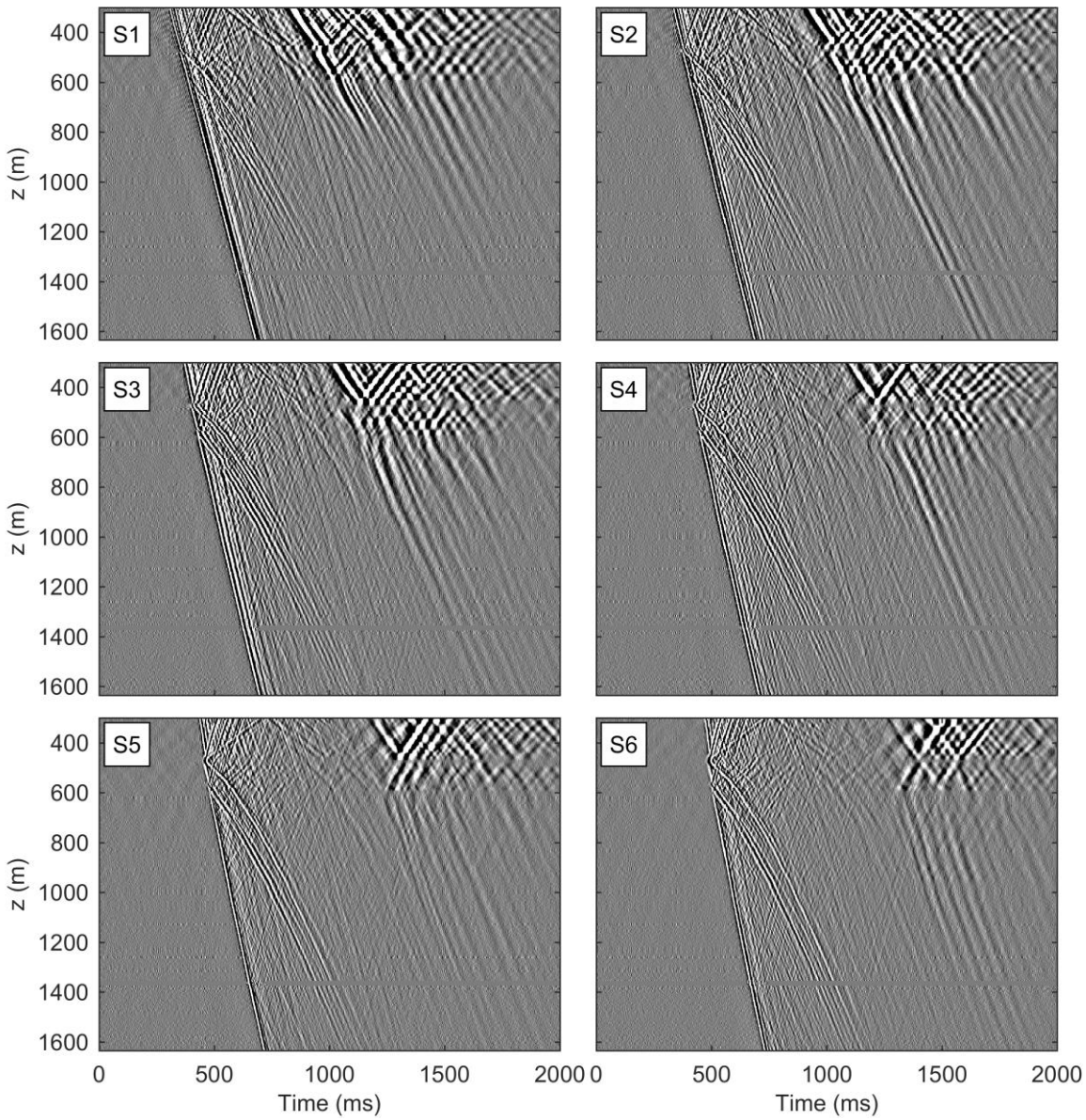

Figure 2. Raw DAS gathers used in the inversion.

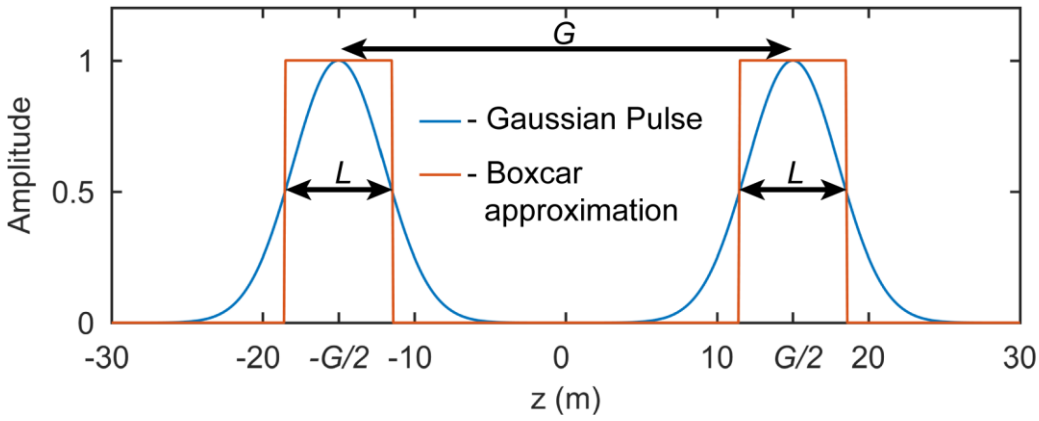

Figure 3. Schematic of DAS measurement. G is the gauge length, L is the pulse width.

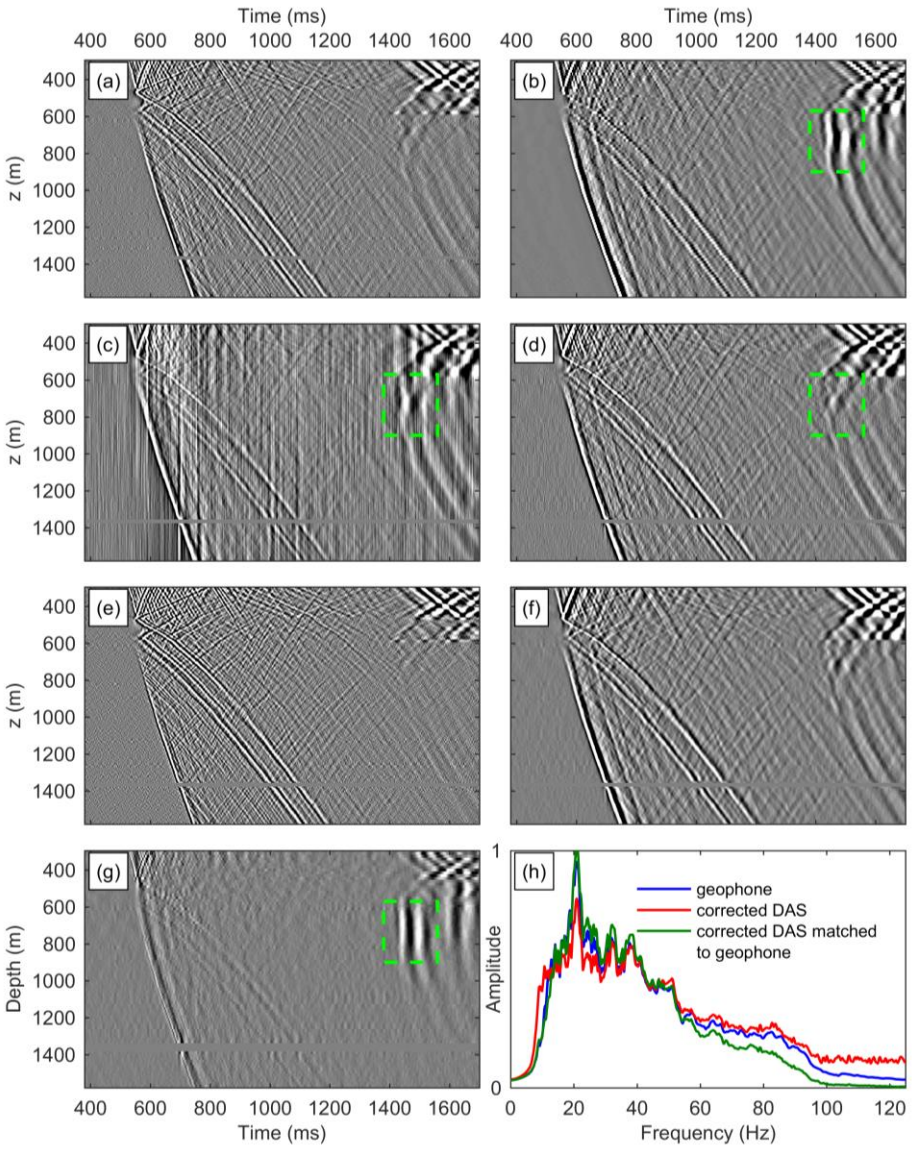

Figure 4. Comparison of DAS and vertical geophone gathers. Raw DAS gather (a); vertical geophone gather (b); DAS gather after conversion with $\gamma = 0$ (c), $\gamma = 0.0005$ (d), $\gamma = 0.05$ (e); DAS gather after conversion with $\gamma = 0.0005$ matched to geophone gather using a Wiener filter (f); difference between the geophone gather 4b and corrected matched DAS gather 4f decimated to geophone trace interval (g); and comparison of average amplitude spectra of gathers displayed in subplots 4b, 4d and 4f (h). The green box outlines an S-wave event which is not correctly recovered by the regularized conversion due to its low k_z value.

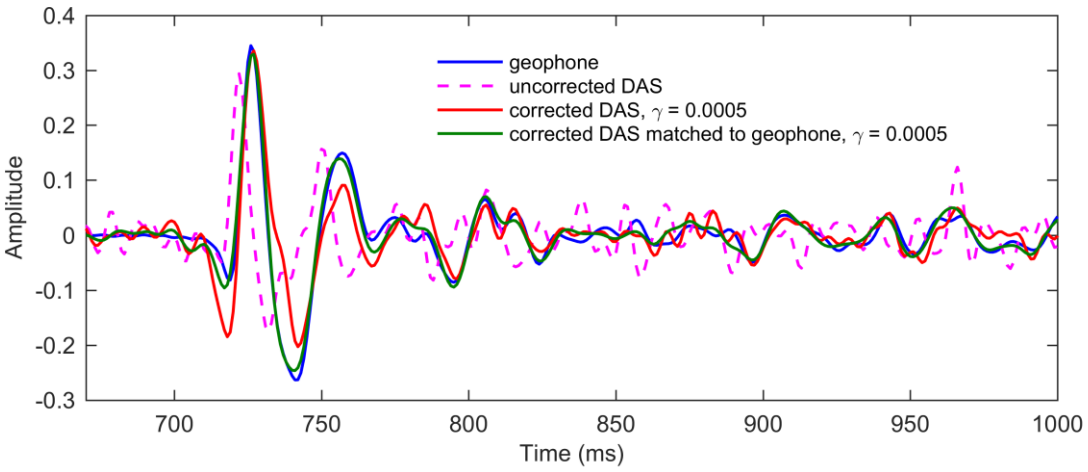

Figure 5. Comparison of geophone and DAS traces at the depth of 1500 m from Figure 4.

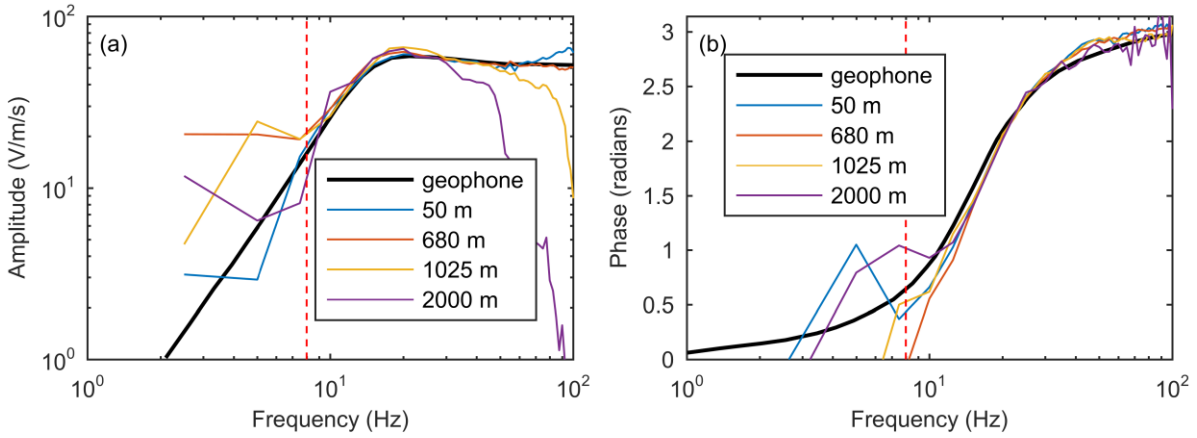

Figure 6. Comparison of amplitude (a) and phase (b) characteristics of the shaping filters for several shots of the survey (offsets of these shots are shown in the legend) and the amplitude and phase characteristics of the vertical geophones with 15 Hz natural frequency. For comparison, amplitude characteristics of the shaping filters were scaled with a constant scaling coefficient.

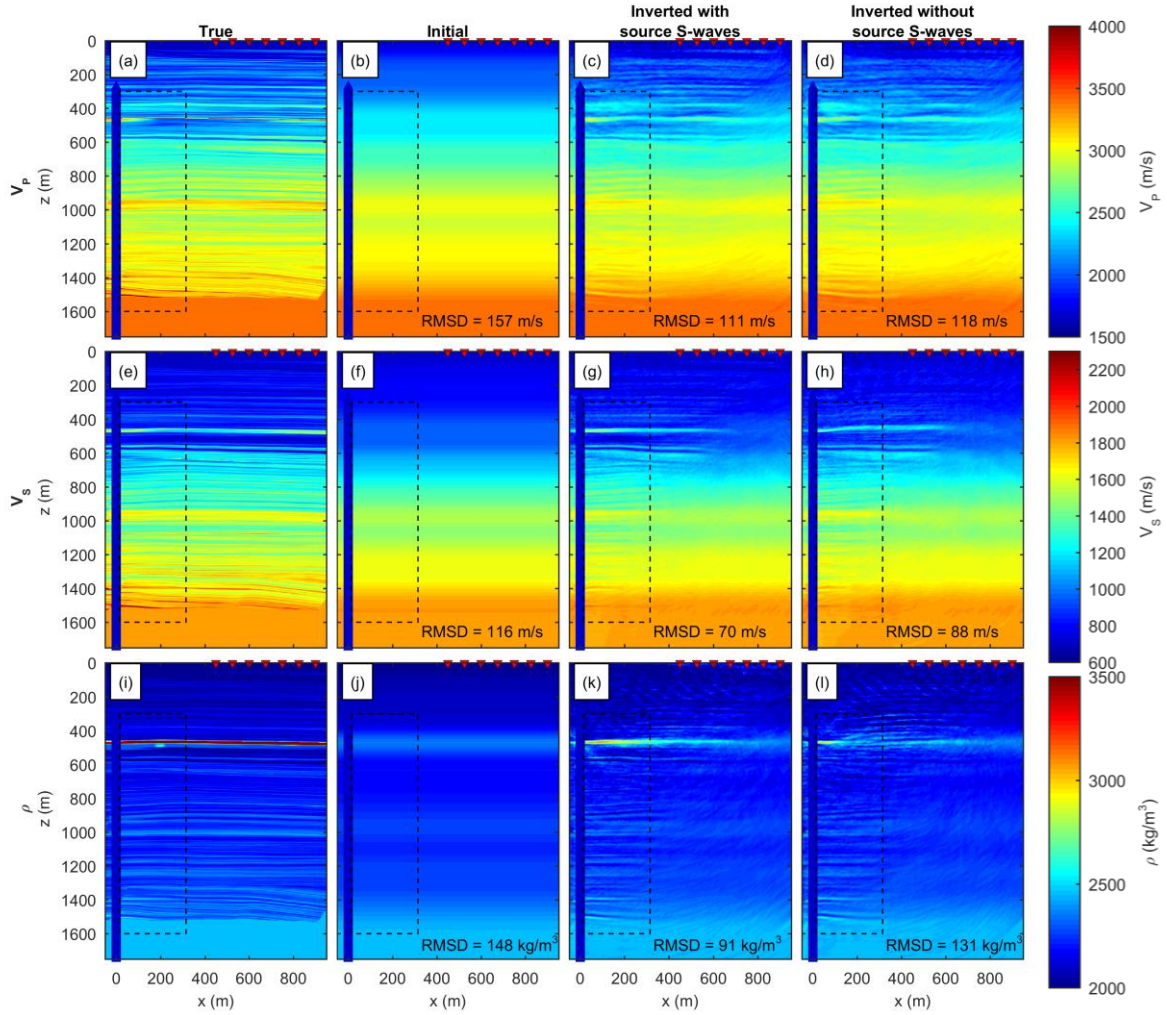

Figure 7. Inversion of synthetic data. V_P (a-d), V_S (e-h), and density (i-l) models of the subsurface: true (a, e and i), initial (b, f and j), inverted with source S-waves (c, g and k), and inverted without source S-waves (d, h and l). Source and receiver locations are overlayed on the models. RMSD values calculated in the displayed window are shown for each model.

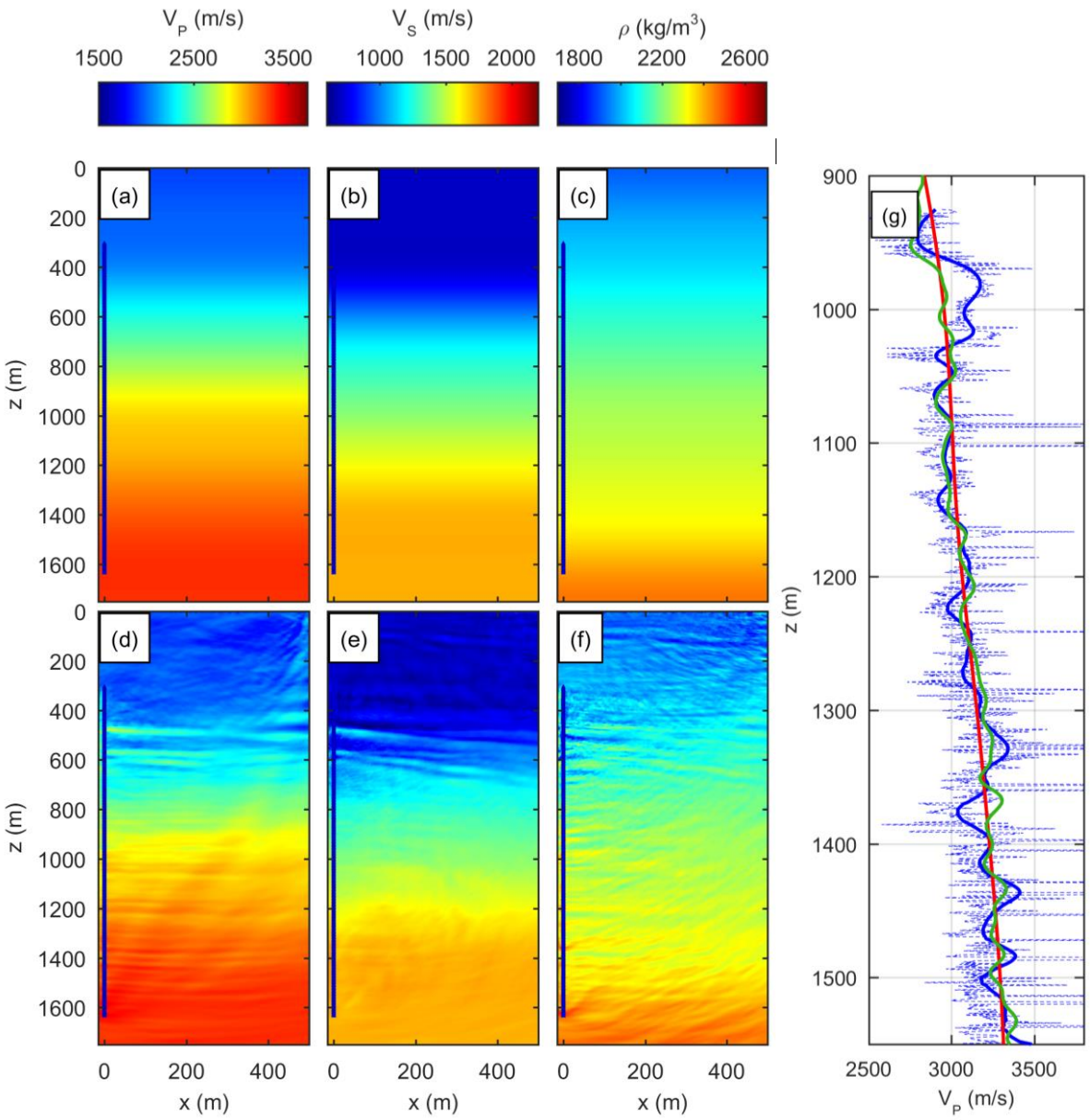

Figure 8. Inversion of field data. Initial (a-c) and inverted (d-f) V_P (a, d), V_S (b,e), and density (c,f) models of the subsurface and a comparison of inverted V_P model 5 m away from the well with the available log data (g). In (g), V_P log is a dashed blue line, V_P log smoothed to approximate resolution of the inversion is a solid blue line, V_P starting model is shown in red and the V_P inverted model is shown in green. Receiver locations are overlayed on the models.

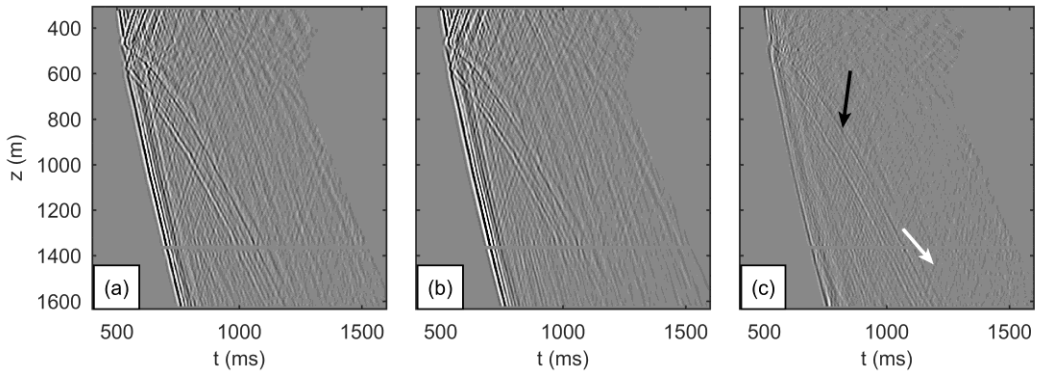

Figure 9. Converted DAS field gather at maximum inversion frequency (a), synthetic gather calculated in the final inverted model (b), and the misfit (c). On the misfit plot, the S-waves (black arrow) and the upgoing waves from below the wellbore (white arrow) have highest amplitudes